

Time-resolved tracking of a sound scatterer in a complex flow: Nonstationary signal analysis and applications

Nicolas Mordant and Jean-François Pinton^{a)}

École Normale Supérieure de Lyon & CNRS UMR 5672, Laboratoire de Physique, 46 allée d'Italie, F-69364 Lyon, France

Olivier Michel

Laboratoire d'astrophysique & CNRS UMR 6525, Université de Nice, Parc Valrose, F-06108 Nice, France

(Received 1 November 2000; revised 4 December 2001; accepted 4 February 2002)

It is known that ultrasound techniques yield nonintrusive measurements of hydrodynamic flows. For example, the study of the echoes produced by a large number of particles insonified by pulsed wavetrains has led to a now-standard velocimetry device. In this paper, a new technique for the measurement of the velocity of individual solid particles moving in fluid flows is proposed. It relies on the ability to resolve in time the Doppler shift of the sound scattered by the continuously insonified particle. For this signal-processing problem two classes of approaches can be used: time-frequency analysis and parametric high-resolution methods. In the first class the spectrogram and reassigned spectrogram is considered, and applied to detect the motion of a small bead settling in a fluid at rest. In nonstationary flows, methods in the second class are more robust. An approximated maximum likelihood (AML) technique has been adapted, coupled with a generalized Kalman filter. This method allows for the estimation of rapidly varying frequencies; the parametric nature of the algorithm also provides an estimate of the variance of the identified frequency parameters. © 2002 Acoustical Society of America. [DOI: 10.1121/1.1477932]

PACS numbers: 43.30.Es, 43.60.-c, 47.80.+v, 43.60.Qv [DLB]

I. INTRODUCTION

Our original motivation stems from the need of a technique to measure the velocity of individual tracer particles in complex flows, and thus to be able to study hydrodynamics in the Lagrangian frame of reference. Indeed, the Lagrangian dynamics governs the physics of transport, mixing, and the Eulerian complexity of chaotic and turbulent flows. Lagrangian studies have been made in numerical experiments where chaotic¹ and turbulent²⁻⁵ flows have been considered. For turbulence, the numerical studies are limited to small Reynolds number flows. Although experimental measurements are much needed, few Lagrangian methods have been developed. The main ones rely on optical techniques: tracking features have been adapted to particle image velocimetry measurements⁶ and fast detectors have been used to image short particle tracks and measure particle accelerations.⁷ In the first case the time resolution is low (60 frames per second) and in the second case the volume in space sampled is small ($\sim 1 \text{ mm}^3$). Inspired by sonar principles, we propose an acoustic method that can resolve single-particle motion over extended regions of a space ($\sim 1000 \text{ cm}^3$) with a high time resolution (1 ms). The main advantages of our technique are: (i) the particle velocity is measured directly and not as a derivative of position (always quite noisy); (ii) the acoustic detection samples a larger region of space than optical devices and can record particle motion for longer times than high-speed cameras; (iii) it can be used in nontransparent media. The principle is to monitor the Doppler shift of the sound scattered by a particle which is *continuously* insoni-

fied. This is an extension of the pulsed Doppler principle that has been developed to measure velocity profiles and that has many applications in fluid mechanics and medicine.⁸ The continuous insonification improves the time resolution of the measurement, although it limits the tracking to a very small number of particles.

The measurement relies on the ability to track a Doppler frequency and its variation in time. For this signal-processing problem two classes of approaches have been developed: (i) time-frequency analysis and (ii) high-resolution parametric spectral analysis. Time-frequency methods rely mainly upon the quadratic Wigner-Ville transform, or smoothed versions of it. Numerous studies and papers have recently been published, in which the theoretical issues are presented (see, e.g., the textbooks by Flandrin⁹ or Cohen¹⁰). These nonparametric techniques are convenient and well-suited for weakly nonstationary signals with a good signal-to-noise ratio (SNR). However, time-frequency representations present numerous drawbacks when it comes to extracting trajectory information. Their quadratic nature gives rise to numerous spurious interference terms that require postprocessing. For signals with a faster frequency modulation and a low SNR, we show here that an optimized parametric approach is a better choice. Parametric high-resolution spectral analysis methods take advantage of an *a priori* knowledge of the spectral content of the recorded signal, namely the emitted signal frequency plus one or many Doppler-shifted echoes. Furthermore, a time-recursive frame for the estimation of the Doppler shift is proposed here, where the evolution of the frequency is taken into account in the algorithm.

The two methods are tested in two experiments, in which the acoustic signals have different time scales and

^{a)}Electronic mail: pinton@ens-lyon.fr

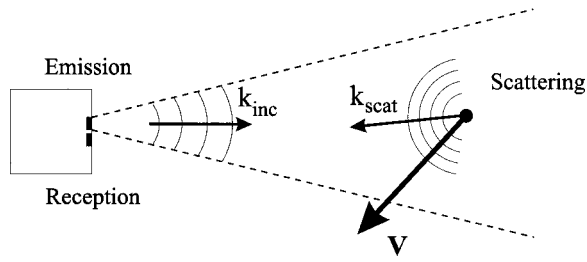


FIG. 1. Principle of measurement. A large 3D measurement zone is achieved by using a transducer size of a few wavelengths.

noise levels. The first experiment is a study of the transient acceleration of a heavy sphere settling under gravity in a fluid at rest. This situation addresses the fundamental problem of the response of a solid particle to a step force. The characteristic time scale of velocity variations is slow ($\tau \sim 50$ ms) and the signal-to-noise ratio is fair (about 20 dB); we show that a technique of reassignment of the spectrogram gives good results. The second experiment deals with the motion of a small, neutrally buoyant sphere embedded in a turbulent flow. In this case the fundamental issue is that of the Lagrangian velocity fluctuations. There, velocity variations occur over times of about 1 ms and the signal-to-noise ratio is low (less than 6 dB). We show that the approximate maximal likelihood (AML) parametric method yields very good results in that situation. Altogether, our techniques yields a direct measurement of the velocity of single particles in complex fluid flows. It allows investigation of experimentally fundamental issue in fluid dynamics (the study of flow motion in the Lagrangian frame) and has potential applications in fields such as engineering (transport and mixing) and biomedicine (the tracking of implants).

The paper is organized as follows: in Sec. II we present the acoustic technique and measurement procedure. In Sec. III we describe the signal-processing techniques, with a particular emphasis on the approximate maximum likelihood (AML) method, which has been developed and optimized to this particle tracking problem. Examples of applications to measurements in real flows are given in Sec. IV.

II. ACOUSTICAL SETUP

A. Principle of the measurement

In the experimental technique proposed here, a particle is continuously insonified. It scatters a sound wave whose frequency is shifted from the incoming sound frequency due to the Doppler effect. This Doppler shift is directly related to the particle velocity \mathbf{v}_p

$$\Delta\omega = \mathbf{q} \cdot \mathbf{v}_p, \quad (1)$$

where \mathbf{q} is the scattering wave vector (the difference between the incident and scattered wave vectors $\mathbf{q} = \mathbf{k}_{\text{scat}} - \mathbf{k}_{\text{inc}}$) and ω is the wave pulsation.

We choose a backscattering geometry (see Fig. 1) so that $\mathbf{q} = -2\mathbf{k}_{\text{inc}}$ and the frequency shift becomes

$$\Delta\omega(t) = -2 \frac{v(t)}{c} \omega_0, \quad (2)$$

where c is the speed of sound, ω_0 is the incident pulsation, and $v(t)$ is the component of the velocity on the incident direction at time t . We continuously insonify the moving particle and record the scattered sound. If need be, the particle position can be obtained by numerical integration of the velocity signal.

B. Transducer characteristics and acquisition

The transducers are made of two piezoelectric elements of size 2×2 mm each, separated by $100 \mu\text{m}$. Their resonant frequency is about 3.2 MHz and their bandwidth at -3 dB is 1.5 MHz. Sound emission is set at 3 or 3.5 MHz; experiments are performed in water so that the wavelength is $\lambda = 0.50$ or 0.43 mm. The corresponding emission cone for each $d = 2$ -mm-square element is 29° at 3 MHz and 24° at 3.5 MHz. In our measurements, the particle to transducer distance lies between 5 and 40 cm, so that measurements are made in the far field ($d^2/\lambda > 10$ mm). Given maximum flow and particle velocities of the order of $1.5 \text{ m} \cdot \text{s}^{-1}$, we expect a maximum sound-frequency shift of the order of 5 or 6 kHz, depending on whether the emission is at 3 or 3.5 MHz. This yields a frequency modulation rate of at most 0.25%. One transducer is used for continuous sound emission and the other for scattered sound detection. As the operation is continuous (as opposed to pulsed) and the elements are located close to one another, we observe a coupling between the emitter and the receiver of the order of 60 dB (this is due both to electromagnetic coupling and to acoustic surface waves cross talk).

When connected to a $50\text{-}\Omega$ impedance, the acoustic transducers yield an electrical signal of about 8 mV. This signal is mainly due to the electromagnetic coupling with the emitter. The part of the signal due to the acoustic scattering from the moving particle is of the order of 2 to $30 \mu\text{V}$ —for comparison, the noise is $1 \mu\text{V}$. Hence, the signal-to-noise ratio is between 0 and 30 dB. The transducer output is sampled at 10 MHz over a 21-bit dynamical range (input range 31.25 mV) and numerically heterodyned at the emitting frequency. It is then decimated at the final sampling frequency of 19 531 Hz. The acquisition device is an Agilent hpe1430A VXI digitizer.

C. Scattering by an elastic sphere

The study of sound scattered by a fixed solid sphere is a classic but continuing area of study, and difficulties arise in the interpretation of observed phenomena especially when trying to deal with elasticity and absorption.^{11–13} Complex behavior is observed linked with resonances of Rayleigh waves at the surface of the sphere. As a consequence, the scattered pressure distribution varies both in directivity and amplitude. A generic expression for the far-field pressure is the following:

$$P_{\text{scat}}(r, \theta) = P_{\text{inc}} \frac{af(ka, \theta)}{2r} e^{ikr}, \quad (3)$$

where r is the distance from the center of the sphere, a its radius, P_{inc} the incident pressure on the sphere, k the incident wave number in the fluid, θ the scattering angle, and f is a

form function which depends on the physical properties of the solid medium. Under very general assumptions, f can be expressed analytically.¹¹ Physically, f represents the sum of the specular echo and of interferences due to the radiation by Rayleigh waves.^{12,13} As a result, f is a strongly varying function, particularly for high values of ka . In our experiments we used spheres of different material (polypropylene PP, steel, tungsten carbide, glass) with corresponding ka between 7 and 15. The flow acts on the sphere motion, thus causing its acceleration and, eventually, its rotation. These effects may change the radiation diagram: first, there is Doppler shift for the sound received by the sphere, and, perhaps more importantly, the sphere rotation may change the Rayleigh emission. For these reasons, the evolution of the amplitude of the scattered sound during the particle motion is quite complex. However, the observed amplitude modulation varies slowly enough to allow a correct estimate of the frequency modulation of the scattered sound (see the times series presented in Sec. IV).

III. SIGNAL PROCESSING

Numerous spectral estimation techniques are based on the ideas behind Fourier analysis of linear time-invariant (LTI) differential equations. These techniques may be divided into (i) nonparametric techniques where the basis functions are implicitly the harmonically related complex exponentials of Fourier analysis, and (ii) parametric techniques whose task is the estimation of the parameters of a (sub)set of complex exponentials. The spectrogram and the reassigned spectrogram belong to the former category, whereas the maximum likelihood and its approximate form belong to the latter.

A. Time-frequency analysis

The most common time-frequency distribution (TFD), the spectrogram, involves a moving time window. This window attempts to capture a portion of the signal which is sufficiently restricted in time so that stationarity and LTI assumptions are approximately met. To overcome the inherently poor localization in the time-frequency plane, a method has been proposed by Gendrin *et al.*,¹⁴ and extended more recently by Auger and Flandrin.^{9,15} The idea is to locally reassign the energy distribution to the local center of gravity of the Fourier transform. Despite its ability to exhibit clear and well-localized trajectories in the time-frequency plane, this technique requires an additional image-processing step to extract the TF trajectory. For rapidly fluctuating frequency modulations and/or low SNR, spurious clusters appear which makes this extraction difficult. The parametric method presented below is more robust.

B. Parametric spectral estimation based on approximate likelihood

This approach is based upon maximum likelihood spectral estimation (see, e.g., Kay¹⁶). The fundamentals are briefly recalled, as they serve as a basis for the approximate likelihood scheme, originally developed by Clergeot and Tressens.¹⁷ This work is extended here within a recursive

estimation frame, thus allowing us to track the variations of the Doppler frequency shift induced by fast velocity changes of a scattering sphere imbedded in a turbulent flow. Michel and Clergeot have developed a similar approach for nonstationary spectral analysis in an array processing frame.^{18,19}

1. Introduction

In this section, we address the problem of estimating an unknown number M of frequencies (unknown parameters in the sequel) f_1, \dots, f_M in a signal embedded in noise. We assume that the signal has the following structure:

$$x(t) = y(t) + n(t)$$

$$= \sum_{m=1}^M a_m(t) \exp(j(2\pi f_m t + \phi_m)) + n(t). \quad (4)$$

Note that this model assumes that the signal is analytical; experimentally this is the case since data are obtained via passband (lock-in) sampling using the modulus and the phase of the acoustic wave. The time series is regularly sampled with time period T_s , so as to insure $1/T_s > 2f_{\max}$ where f_{\max} stands for the bandwidth of the antialiasing filter used in the recording process.

The method relies upon the identification of a signal subspace (respectively, noise subspace). At infinite signal-to-noise ratio (SNR), this subspace is spanned by the M spectral lines; its identification requires us to build an observation space of dimension $M+1$ at least. To this end, we introduce a set of Q K -dimensional observation vectors ($Q > K > M$):

$$\mathbf{Y}(t_j) = [y(t_j), y(t_j+1), y(t_j+2), \dots, y(t_j+(K-1))]^T$$

$$j = 1, \dots, Q. \quad (5)$$

In this expression the t_j are chosen such that the \mathbf{Y} vectors are linearly independent and the sampling frequency is set to $T_s = 1$, and the term *frequency* will refer to *normalized* frequency (i.e., the actual frequency, divided by $F_s = 1/T_s$).

The signal \mathbf{Y} is completely defined by its constitutive frequencies and corresponding amplitudes (deterministic but unknown)

$$F = \{f_1, \dots, f_M\}$$

$$\mathbf{A} = [a_1 \exp(j\phi_1), \dots, a_M \exp(j\phi_M)]^T$$

$$\mathbf{S}(\mathbf{F}) = [\mathbf{S}_1, \dots, \mathbf{S}_M] \quad (6)$$

$$= \begin{pmatrix} 1 & \exp(2\pi f_1) & \cdots & \exp(2\pi(K-1)f_1) \\ \vdots & & & \vdots \\ 1 & \exp(2\pi f_M) & \cdots & \exp(2\pi(K-1)f_M) \end{pmatrix}^T,$$

$$\mathbf{Y} = \mathbf{S}(\mathbf{F})\mathbf{A}.$$

Under the infinite SNR assumption, the signal subspace is completely identified and the M frequencies are easily calculated.¹⁶ However, we wish to build a method that handles situations of low SNR, for which the available observations are $\mathbf{X} = \mathbf{Y} + \mathbf{N}$, where \mathbf{N} is an additive noise vector, statistically independent of the signal. We assume that it is complex, white Gaussian circular and iid (independent increment identically distributed) with (unknown) variance σ^2 .

The distribution function of a k -dimensional vector \mathbf{N} defined by

$$\mathbf{N}(t) = [n(t), n(t+1), n(t+2), \dots, n(t+(K-1))]^T, \quad (7)$$

reads

$$p(\mathbf{N}) = \frac{1}{(\sqrt{2\pi}\sigma)^K} \exp\left(-\frac{|\mathbf{N}|^2}{2\sigma^2}\right). \quad (8)$$

In the following, the term *observation* refers to a set of Q K -dimensional vectors \mathbf{X} :

$$\begin{aligned} \mathbf{X}(t_j) &= [x(t_j), x(t_j+1), x(t_j+2), \dots, x(t_j+(K-1))]^T, \\ j &= 1, \dots, Q. \end{aligned} \quad (9)$$

One observation is thus associated with a time window of length $K+Q-1$ —the actual duration of one observation is $T_{\text{obs}} = (Q+K-2)T_s$. Although we aim at identifying frequency fluctuations, we assume that the frequency parameters f_1, \dots, f_M remain constant over the duration of one observation. This implies that the physical signal is oversampled. Under the assumption that the noise process is iid, the log likelihood of a subset of Q' independant realizations of \mathbf{X} is given by

$$\begin{aligned} \mathcal{L}(\mathcal{P}) &= -KQ' \log(2\pi\sigma^2) \\ &\quad - \frac{1}{2\sigma^2} \sum_{q=1}^{Q'} |\mathbf{X}(q) - \mathbf{S}(\mathbf{F})\mathbf{A}(q)|^2. \end{aligned} \quad (10)$$

According to the maximum likelihood principle, the set \mathcal{P} of parameters must be chosen in order to maximize expression (10).

2. Reduced expression

Minimizing (10) jointly for all the parameters is usually untractable. Most authors propose a separate maximization for each of the parameters. For our application, the spectral components (i.e., \mathbf{A} and \mathbf{F}) are the relevant variables. We first maximize with respect to \mathbf{A} and derive an expression for the optimal \mathbf{F} ; σ^2 is estimated independently.

The value of vector \mathbf{A} which minimizes the norm $|\mathbf{X}(q) - \mathbf{S}(\mathbf{F})\mathbf{A}(q)|^2$ is easily obtained

$$\mathbf{A}(q) = (\mathbf{S}^+ \mathbf{S})^{-1} \mathbf{S}^+ (\mathbf{F}) \mathbf{X}(q). \quad (11)$$

Note that the “signal only” vector $\mathbf{Y} = \mathbf{X} - \mathbf{N}$ appears to be the orthogonal projection of \mathbf{X} on the signal subspace spanned by the row vectors of \mathbf{S}

$$\mathbf{Y} = \mathbf{S}(\mathbf{F}) \cdot \mathbf{A}(q) = \mathbf{S}((\mathbf{S}^+ \mathbf{S})^{-1} \mathbf{S}^+ (\mathbf{F}) \mathbf{X} = \Pi_s(\mathbf{F}) \mathbf{X}, \quad (12)$$

where $\Pi_s(\mathbf{F})$ stands for the parametric projector on the signal subspace.²¹ Let $\Pi_n(\mathbf{F}) = \mathbf{I} - \Pi_s(\mathbf{F})$ be the noise subspace, \mathbf{I} is the identity matrix. By substituting (12) and using the definition of $\Pi_n(\mathbf{F})$ in the expression of the log likelihood (10), one gets the following simplified expression to minimize:

$$L(\mathbf{F}) = \frac{1}{\sigma^2} \sum_{q=1}^Q |\Pi_n(\mathbf{F}) \mathbf{X}(q)|^2. \quad (13)$$

Using the properties of the trace operator (hereafter denoted Tr) and those of the projection matrix $\Pi_n(\mathbf{F})$, the maximum likelihood estimation of \mathbf{F} takes the common form: minimize

$$L(\mathbf{F}) = \frac{Q}{\sigma^2} \text{Tr}[\Pi_n(\mathbf{F}) \hat{\mathbf{R}}_x], \quad (14)$$

where $\hat{\mathbf{R}}_x$ is an estimate of the correlation matrix \mathbf{R}_x of the vector process $\mathbf{X}(q)$. Minimizing $L(\mathbf{F})$ in (14) leads to the exact value \mathbf{F}_{ML} , which has the maximum likelihood. The actual vectors \mathbf{X} are obtained by time shift over the recorded time series; therefore, the observed vectors may not be considered as being corrupted by independent realizations of the noise process, as some “time integration” is performed in the estimation of \mathbf{R}_x . The consequences and interest of such smoothing have been studied by Clergeot and Tressens,¹⁷ and Ouamri,²⁰ in the frame of array processing (in this context, time integration becomes “spatial smoothing”). In the remainder of this paper, the development is based on Eq. (14), no matter how \mathbf{R}_x is estimated; see the Appendix for the practical implementation.

3. Approximate maximum likelihood

Equation (14) is still too complicated to be solved analytically in a simple way. A minimization can be easily performed if $L(\mathbf{F})$ has a quadratic dependance in \mathbf{S} .¹⁷ Let \mathbf{R}_y be the correlation matrix of the signal vectors $\mathbf{Y}(q)$, the assumption that signal and noise are independent allow to establish the following equalities:

$$\hat{\mathbf{R}}_x = \mathbf{R}_y + \hat{\sigma}^2 \mathbf{I}, \quad (15)$$

$$\mathbf{R}_y = \mathbf{S} \mathbf{P} \mathbf{S}^+, \quad (16)$$

$$\mathbf{P} = \mathcal{E}[\mathbf{A} \mathbf{A}^+], \quad (17)$$

where \mathcal{E} stands for the mathematical expectation.

Substituting in Eq. (14) leads to

$$L(\mathbf{F}) = \frac{Q}{\hat{\sigma}^2} \text{Tr}[\Pi_n(\mathbf{F}) \hat{\mathbf{S}} \mathbf{P} \hat{\mathbf{S}}^+]. \quad (18)$$

Clergeot and Tressens¹⁷ propose a second-order approximation of $L(\mathbf{F})$

$$L_{\text{AML}}(\mathbf{F}) = \frac{Q}{\hat{\sigma}^2} \text{Tr}[\hat{\Pi}_n \mathbf{S}(\mathbf{F}) \hat{\mathbf{P}} \mathbf{S}^+(\mathbf{F})], \quad (19)$$

in which $\hat{\Pi}_n$ is estimated by computing the projector spanned by the $(K-M)$ smallest eigenvalues of the estimated covariance matrix $\hat{\mathbf{R}}_x$. They prove that this approach leads to more reliable estimates of \mathbf{F} at low SNR, and that the minimization of L_{AML} is asymptotically efficient. In practice, the following set of equations is used:

$$\hat{\sigma}^2 = \frac{1}{K-M} \text{Tr}(\hat{\Pi}_n \hat{\mathbf{R}}_x), \quad (20)$$

$$\Pi_s(\mathbf{F}) = \mathbf{S}(\mathbf{F}) (\mathbf{S}^+(\mathbf{F}) \cdot \mathbf{S}(\mathbf{F}))^{-1} \cdot \mathbf{S}^+(\mathbf{F}), \quad (21)$$

$$\mathbf{S}(\mathbf{F}) \cdot \hat{\mathbf{P}} \cdot \mathbf{S}^+(\mathbf{F}) = \Pi_s(\mathbf{F}) (\hat{\mathbf{R}}_x - \hat{\sigma}^2 \mathbf{I}) \cdot \Pi_s(\mathbf{F}). \quad (22)$$

The approximately quadratic dependence of L_{AML} in $\mathbf{S}(\mathbf{F})$, allows a fast convergence of the minimization algo-

rithm by using a simple Newton–Gauss algorithm

$$\mathbf{F}(k+1) = \mathbf{F}(k) - \mathbf{H}^{-1} \cdot \mathbf{grad}(L_{\text{AML}})|_{\mathbf{F}=\mathbf{F}(k)}, \quad (23)$$

where k stands for the iteration step in the minimization process, \mathbf{grad} and \mathbf{H} are the gradient and Hessian, respectively (see the expressions in the Appendix).

Let us emphasize that in the previous expression, the recursion applies at a given time, and converges towards the frequency estimate for a unique observation window. The manner in which consecutive estimates are obtained by sliding the window in time and integrating new measurements is addressed in the next paragraph.

4. Combining new measurements and estimates

In this section, it is assumed that new measurements do not allow by themselves the derivation of a good estimate. The variance of such an estimate varies as $1/T_{\text{obs}} \cong (K+Q-1)^{-1}$, whereas integrating new measurements to this estimate allow a better estimation. Let $\hat{\mathbf{F}}(t)$ be an estimate of \mathbf{F} at time t , and $\mathcal{N}(\hat{\mathbf{F}}(t), \Gamma(t))$ its probability density, assumed to be normal with variance $\Gamma(t)$.²² If a linear evolution model is known for $\mathbf{F}(t)$, one has

$$\mathbf{F}(t+1) = \mathbf{M}\mathbf{F}(t) + \varepsilon(t), \quad (24)$$

$$p_{t+1|t}(\mathbf{F}) = \mathcal{N}(\hat{\mathbf{M}}\mathbf{F}(t), \hat{\mathbf{M}}\Gamma(t)\mathbf{M}^+ + \mathbf{R}_\varepsilon), \quad (25)$$

where \mathbf{M} is the evolution matrix, ε is a perturbation term, which is statistically independent from \mathbf{F} , and \mathbf{R}_ε is its covariance matrix. $p_{t+1|t}$ is the probability density function that can be derived for time $t+1$, if the observations are made until time t only. As such an evolution equation is usually unknown, \mathbf{M} will be set to the identity matrix in the rest of the paper (see Michel¹⁹) for a detailed discussion). Applying the Bayes rule over conditional probabilities gives

$$p_{t+1|t+1}(\mathbf{F}) = \frac{p_{t+1|t}(\mathbf{F}) \cdot p_{t+1}(\mathbf{X}|\mathbf{F})}{p_{t+1}(\mathbf{X})}. \quad (26)$$

Noting that $\log(p_{t+1}(\mathbf{X}|\mathbf{F}))$ is the log-likelihood function for which a reduced expression has been derived in the previous section, one gets, after all reductions and identifications, the simple following expressions:

$$\hat{\mathbf{F}}(t+1|t) = \hat{\mathbf{F}}(t), \quad (27)$$

$$\Gamma(t+1|t) = \Gamma(t) + \mathbf{R}_\varepsilon, \quad (28)$$

$$\Gamma(t+1)^{-1} = \mathbf{H} + \Gamma(t+1|t)^{-1}, \quad (29)$$

$$\hat{\mathbf{F}}(t+1|t+1) = \hat{\mathbf{F}}(t+1) = \hat{\mathbf{F}}(t+1|t) - \Gamma(t+1)^{-1} \cdot \mathbf{grad}, \quad (30)$$

where it can be shown that the gradient function has the same expression as in the previous section. The expression for \mathbf{grad} is given in the Appendix. \mathbf{R}_ε is an unknown matrix which will be practically set to $v^2\mathbf{I}$, where v^2 will be tuned in order to allow the algorithm to take slight changes in \mathbf{F} into account. Furthermore, it is interesting that the set of expression above expresses a generalized Kalman filter for estimating \mathbf{F} (in the sense that it relies upon second-order expansion of the log-likelihood functions). The statistical convergence properties and numerical efficiency of these ap-

proaches are described in the work of Michel and Clergeot¹⁸ and Michel.¹⁹

IV. EXPERIMENTAL RESULTS

We first describe the simple case of a particle settling in a fluid at rest. It is well adapted to the reassigned spectrogram method because the acoustic signal has a good SNR and a slow frequency modulation. We show that it allows the extraction of the subtle interaction between the falling particle and its wake. We then study the more complicated case of the motion of a particle embedded in a turbulent flow, where the dynamics of motion is much faster and the SNR is poor. We show that the AML method is well suited.

A. The settling sphere

1. Motivation and experimental setup

When a particle is released in a fluid at rest, its developing motion creates a wake. The particle velocity is then set by the balance between buoyancy forces and drag, and additional subtle effects: first, “added mass” corrections because the particles “pushes” the fluid, and second, a “history” force because the wake reacts back on the particle. Formally, one can write the equation of motion as^{23–25}

$$\left(m_p + \frac{1}{2}m_f\right) \frac{d\mathbf{v}_p}{dt} = (m_p - m_f)\mathbf{g} - \frac{1}{2}\pi a^2 \rho_f \|\mathbf{v}_p\| \mathbf{v}_p c_D(\text{Re}) + \mathbf{F}_{\text{history}}, \quad (31)$$

where m_p is the particle mass, m_f is the mass of a fluid particle of the same size, v_p is the particle velocity, \mathbf{g} is the acceleration of gravity, a is the sphere radius, ρ_f is the fluid density, c_D is the static empiric drag coefficient, Re is the Reynolds number $\text{Re} = 2av_p/\nu$ (ν is the fluid’s kinematic viscosity), and $\mathbf{F}_{\text{history}}$ is the so-called history force. In this expression, the drag coefficient is usually obtained from measurement of the forces acting on a body at rest in a hydrodynamic tunnel. The history term, however, is largely unknown. Analytic expression can only be derived in the limit of small Reynolds numbers (less than 10) and cannot be applied for real flow configurations (e.g., multiphase flows) where $\text{Re} \gg 1$.

We perform measurements of the motion of a settling sphere, with the aim of evaluating the influence of the history forces. We use a water tank of size 1.1×0.75 m and depth 0.65 m, filled with water at rest (Fig. 2). The bead is held by a pair of tweezers, 5 cm below the transducers. It is released at time $t=0$ without initial velocity and its trajectory is about 50 cm long. The data acquisition is started before the bead is released in order to capture the onset of motion.

2. Results

Let us use as a first example the fall of a steel bead, 0.8 mm in diameter. A typical time series is shown in Fig. 3. The frequency of the scattered sound is low at the beginning of the fall and increases as the particle accelerates. The amplitude decreases as the distance to the transducer also increases. The Doppler shift during the bead motion is detected

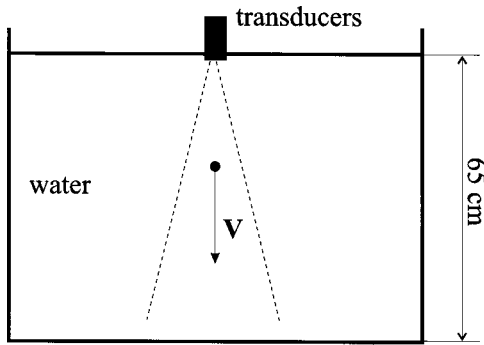


FIG. 2. Experimental setup in the case of the settling sphere. The bead is released 5 centimeters under the transducers, without initial velocity.

using the spectrogram representation and a subsequent reassignment scheme. The simple spectrogram and reassigned version are shown in Fig. 4. The reassignment technique drastically improves the localization of the energy in the time-frequency plane. In this case, the image processing step computes $v_p(t)$ as the line of maxima. The precision of the overall measurement depends on two factors: first on the intrinsic precision of the reassignment method and second on the dispersion of the measurements (the reproducibility of the bead motion over several experiments). The intrinsic precision of the reassignment method has been empirically studied using synthetic signals modeling the particle dynamics plus a noise that mimics the experimental data. We observed that for our choice of parameters (a time-frequency picture with 256×256 pixels) the rms precision is about one half-pixel both in time- and frequency directions. The method thus allows a precise analysis of the dynamics of the fall; we describe below two sets of experiment that illustrate the potential of the reassignment technique.

First, we show in Fig. 5 the velocity of a 1-mm steel bead (averaged over ten falls) together with two numerical simulations based on Eq. (31), first without the memory

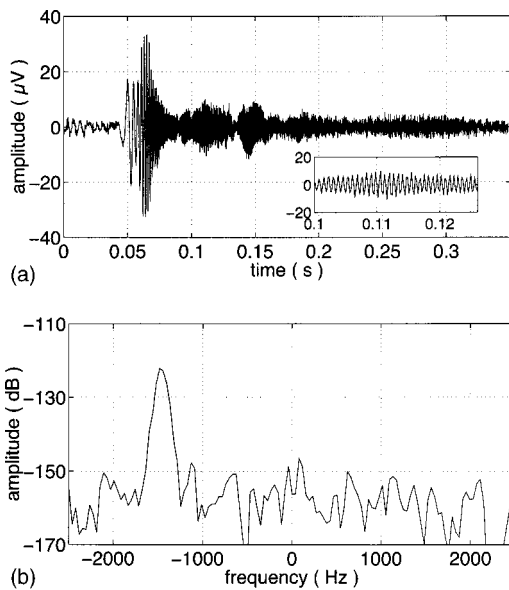


FIG. 3. Data from a steel bead (diameter 0.8 mm) settling in water at rest. (a) Typical time series; (b) power spectral density of the inset figure. On the x axis, zero corresponds to the emission frequency.

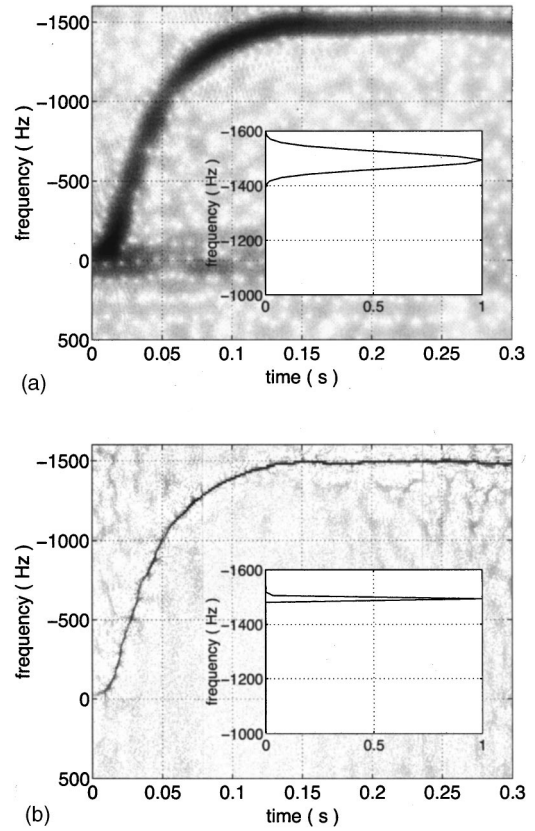


FIG. 4. (a) Spectrogram of the backscattered sound, after heterodyne detection. (b) Reassigned spectrogram. In each figure the inset shows a normalized cross section of the spectrogram. The algorithm is that of the `tftrsp` function of the MATLAB time-frequency toolbox (Ref. 32). To get rid of the spectral components at zero frequency due to the coupling between transducers and at small frequencies around zero due to slow motion of the water surface, we use a high-pass fifth-order Butterworth filter of cutoff frequency 25 Hz (corresponding to a velocity of 5 mm/s). Data of an 0.8-mm steel bead settling in water at rest.

force and second with the expression of the memory force derived at low Reynolds numbers (called the Stokes memory term, as in Maxey and Riley²³). The precision of the detection technique is sufficient for the measured profile to be compared to the simulated curves and to draw physical con-

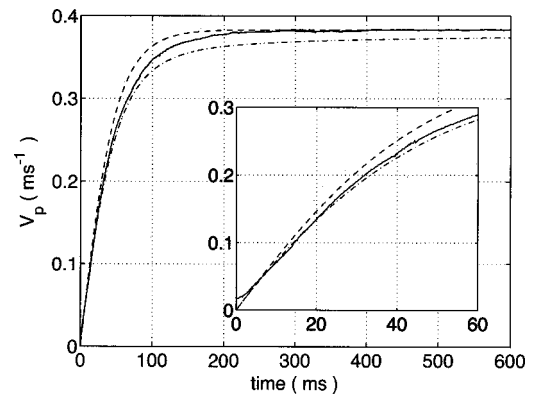


FIG. 5. Velocity measurement of a steel bead of diameter 1 mm (solid line), compared to numerical simulations without memory force (dashed) and with Stokes memory (dash-dotted). The inset shows an enlargement near the onset of motion. The Reynolds number, based on the limit velocity is 430. The sphere velocity profile results from averaging $n=10$ successive experiments.

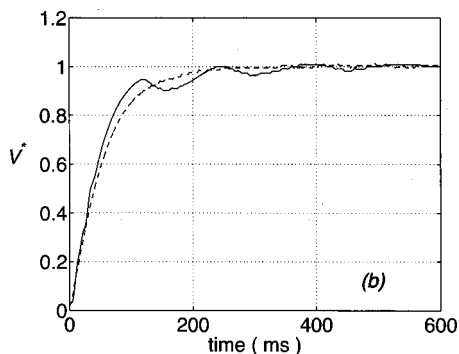


FIG. 6. Fall of a tungsten carbide sphere $D=1$ mm (dashed) compared to a glass bead $D=2$ mm (solid), at $Re \sim 400$. The velocity is nondimensionalized by the limit velocity. Curves are not averaged over several experiments.

clusions about the hydrodynamical forces. At early times, the trajectory is close to the simulation with memory force. This is due to the diffusion away from the bead surface of the vorticity generated at the boundary.^{23–25} However, as the instantaneous Reynolds number increases, the curve deviates from this simple regime: vorticity is advected into the wake. Memory is progressively lost and the sphere reaches a terminal velocity in a finite time, as does the simulation without memory.

The measurement and signal-processing techniques are then tested on a more nonstationary motion, as in the case of a bead whose density is closer to that of the fluid. In this situation a stronger interaction is expected between the particle motion and the development of its wake. Formally, this traces back to differences in the effective inertial mass and buoyancy mass of the particle—see Eq. (31). In Fig. 6, we show the velocity variation for a light glass sphere (density 2.48) compared to a tungsten bead (density 14.8). We observe that the velocity of the glass oscillates before reaching a constant terminal value, whereas the other particle has a regular acceleration. In the case of light beads the hydrodynamic forces may be large enough to overcome the gravity and change the sign of the acceleration. This is linked with the nonstationarity of the wake, as vortex shedding is known to occur for Reynolds number above critical ($Re_c \sim 250$).

B. Turbulent flow: Lagrangian velocity measurement

1. Motivation and experimental setup

Although extensive Eulerian measurements (i.e., performed at a fixed point in space) are available in turbulent flows,²⁶ Lagrangian data are quite scarce.^{6,27} Numerical simulations are the main source of Lagrangian information,²

together with transposition to the time domain of Kolmogorov's mean-field theory, developed for spatial velocity increments. Of particular importance is the Lagrangian velocity autocorrelation function, which plays a central role in the modeling of turbulent dispersion (pollutants, contaminants, flames, cloud formation, etc.). The main models assume an exponential decay

$$\langle v(t)v(t+\tau) \rangle_t = u_{\text{rms}}^2 e^{-\tau/T_L}, \quad (32)$$

with T_L a time scale characteristic of energy injection. This has been suggested by low Reynolds number studies² but not measured directly in a fully turbulent flow. Such a functional form is in agreement with arguments based on Kolmogorov phenomenology: a velocity increment over a time lag τ should depend only on the power injection per unit mass ϵ and the time lag τ itself. Dimensionally, the only possibility is $\langle (v(t+\tau) - v(t))^2 \rangle_t \propto (\epsilon\tau)$, as in Eq. (32), when the time lag τ is much smaller than the time scale of energy injection T_L .

In order to obtain an adequate measurement of the autocorrelation function, one should be able to track tracer particles for times up to the largest time scales that characterize the forcing of the flow. To this end, it is helpful to choose a confined turbulent flow and to study it in the region where the mean velocity is almost null. The turbulent flow that we use is a von Kármán swirling flow: the water is set into motion by two coaxial counter-rotating disks in a cylindrical tank [Fig. 7(a)]. The flow pattern (averaged in time) is made of a differential toroidal velocity and a poloidal recirculation, as shown in Fig. 7(b). In our experiments, the cylindrical vessel has a linear dimension of the order of 20 cm, and with disks rotating at 5 Hz and above, the Reynolds number $Re = 2\pi R^2 f / \nu$ exceeds 10^6 —where $\nu = 0.8910 \cdot 10^{-6} \text{ m}^2 \text{ s}^{-1}$ is the water kinematic viscosity. In the core region considered here, the generated turbulence approximates isotropic and homogeneous conditions and its statistical characteristics are comparable to that of the largest wind tunnel experiments.^{28–30} The time scales of the flow range from the period of rotation of the driving disks, about 100 ms, down to the Kolmogorov dissipative time scale, equal about 0.5 ms.

For the acoustic measurement, we use the same transducers as in the previous experiments, at emitting frequency 2.5 MHz. They are located at the walls, in the median plane, in order to span the central region of the flow—Fig. 7(b) shows the geometry of the measurement zone. The cylinder and the surface of the disks are covered by 3-cm Ureol 5073A and 6414B by CIBA Corp. Its relative density is 1.1 and the sound velocity is 1460 m s^{-1} so that its acoustic

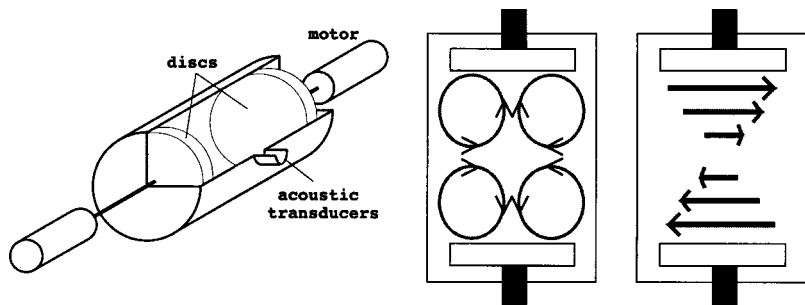


FIG. 7. Experimental setup. The inner radius of the cylinder is 10 cm (disk radius $R=9.5$ cm) and the distance between the disks is 18 cm. They are driven by two 1-kW motors at a constant rotation frequency equal to $f=18$ Hz. The acoustic transducers are placed 18 cm off-axis, in order to increase the volume of the measurement region. The structure of the time-averaged flow is shown in the right two pictures. Each disk creates an azimuthal motion (center picture) and generates a poloidal recirculation (Ref. 33).

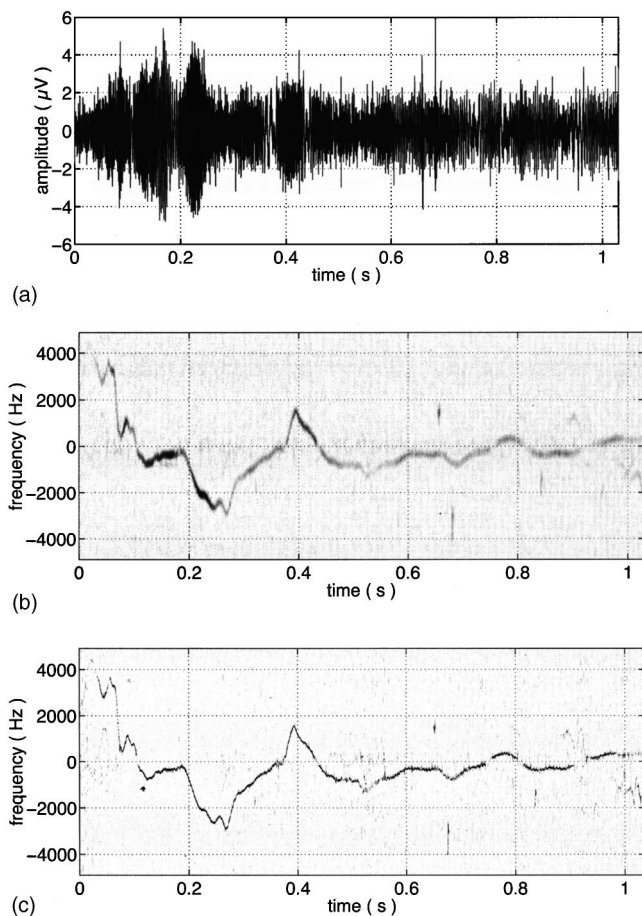


FIG. 8. Sound scattered by a 2-mm diameter PP bead in a turbulent flow at $Re=10^6$. (a) Typical time series; (b) and (c) corresponding spectrogram and reassigned spectrogram.

impedance is close to that of the water, drastically reducing the reflections at the interface water/ureol compared to water/steel. The attenuation at 2.5 MHz is about 6 dB per cm, so that with a 3-cm layer, the total reflection is reduced by a factor of 60. The particle is a polypropylene (PP) sphere of radius 1 mm and relative density 0.9.

If the turbulent motion of the particle is to be tracked, one needs to measure the Doppler shift of the sound scattered with a time resolution of the order of $\delta t \sim 1$ ms. This means that the Doppler shift must be of the order of 1 kilohertz. If one imposes a velocity precision better than 5%, the frequency resolution must be of the order of $\delta f \sim 50$ Hz, so that $\delta t \delta f < 1$. The uncertainty principle implies that time-frequency techniques without *a priori* information about the scattered signal cannot be used in this problem. We show in the next section that a tracking scheme using our high-resolution parametric detection is well adapted.

2. Results

Figure 8 shows (a) a time series; (b) the corresponding spectrogram; and (c) the reassigned spectrogram for the case of one particle in the ultrasonic beam. The signal to noise ratio is very poor, typically less than 6 dB [to give an idea, in Fig. 8(a) the bead enters the ultrasonic beam at $t \sim 20$ ms]. The time-frequency pictures show the trajectory of the particle but the low SNR prevents it from being easily extracted.

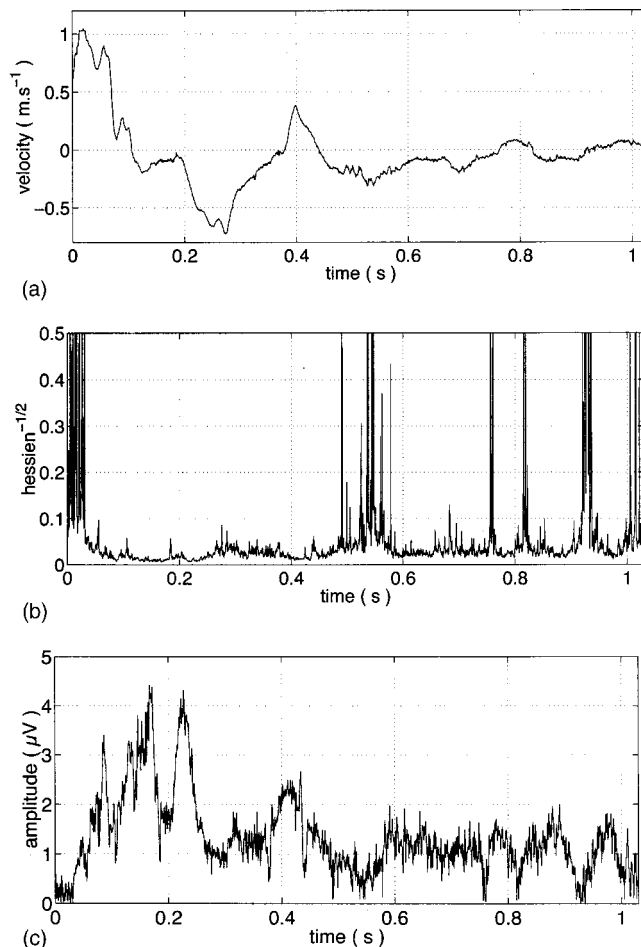


FIG. 9. Output of the AML algorithm for the motion of a 2-mm-diameter PP bead in a turbulent flow at $Re=10^6$. (a) Velocity; (b) corresponding inverse square root of the Hessian; (c) amplitude of the source (the rms value of the noise is $0.9 \mu V$). AML algorithm parameters: $M=1$, $K=7$, $Q=13$, $v^2=10^{-5}$.

In particular, the trajectory in the reassigned picture becomes quite lacunar and extracting it would require sophisticated (and CPU-greedy) image processing techniques.

The result of the AML algorithm is plotted in Fig. 9. The extracted frequency modulation is of course within the estimation in the spectrogram as in Fig. 8(b), but one observes that fine variations in the velocity of the bead are now detected. The algorithm also provides an estimate of the amplitude of the source [Fig. 9(c)]. It can be seen that there is a strong amplitude modulation and that the SNR is at most 6 dB and may become less than 0 dB. As the Hessian is related to the Fisher information matrix,³¹ its inverse square root is linked with the variance of the estimation: a large value of the Hessian indicates an accurate estimation of the modulation frequency and, hence, of the bead velocity. The inverse square root of the Hessian is plotted in Fig. 9(b): very large values are calculated in the absence of a bead in the measurement volume at the beginning and end of the time series (as a signature of the mismatch between the model which is composed of at least one source and the reality: no source). Local lower values (typically less than 0.1) are observed when the variance on the estimation is small. Spurious effects are generated when the frequency modulation ap-

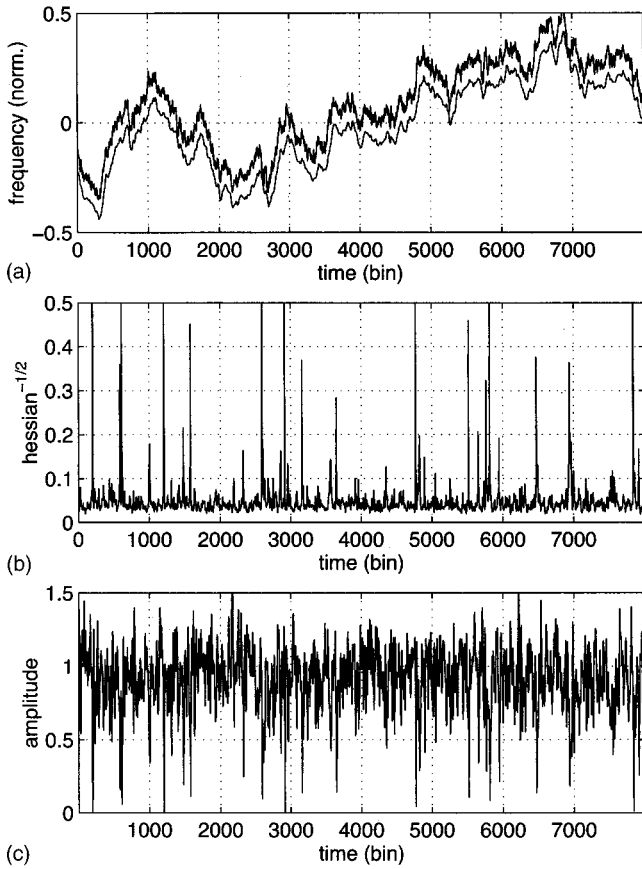


FIG. 10. Test of the AML algorithm on a synthetic signal having the same frequency modulation and SNR as the turbulence data. (a): original (upper curve) and detected (lower curve) frequency modulation—the vertical shift is added for clarity. (b) corresponding inverse square root of the Hessian; (c) amplitude of the source (original set to 1). AML algorithm parameters: $M = 1$, $K = 7$, $Q = 13$, $v^2 = 10^{-5}$.

proaches zero as the Hessian also becomes very small because of the filtering operation done in order to get rid of the coupling part of the signal. Finally, one observes that the Hessian decreases as the signal-to-noise ratio increases (see at time 0.55 s).

In order to test the algorithm, we have applied it to a synthetic signal x_s

$$x_s(j) = \exp\left(2i\pi \sum_{p=1}^j \phi(p)\right) + n(j). \quad (33)$$

The frequency modulation $\phi(p)$ is chosen to mimic the turbulence data: it is made of a Gaussian random variable with a $1/f^2$ time spectrum. The complex white noise n is a random variable with a Gaussian amplitude and a uniformly distributed phase; its variance is equal to 1 so that the SNR in this test is 0 dB. The signal is processed by the AML algorithm with its adjustable parameters tuned to the same values as in the turbulence detection ($M = 1$, $K = 7$, $Q = 13$, $v^2 = 10^{-5}$). The output is shown in Fig. 10. One observes that the detection is very good. The effective low-pass filtering is due to the finite size of the observation window in the estimation of the frequency modulation and to the generalized Kalman filter used in the tracking of its time fluctuations. The inverse Hessian varies as in the turbulence data, with a value mostly lower than 0.1, indicating that the frequency modulation is

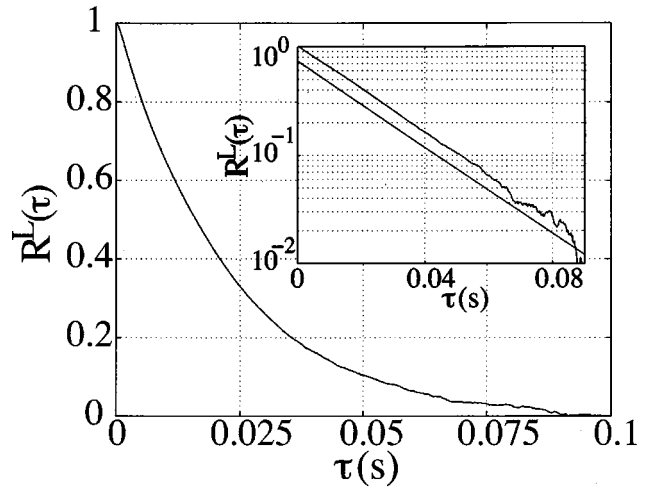


FIG. 11. Velocity autocorrelation coefficient, for a rotation rate of 430 rpm. A best exponential fit is $\rho_v^L(\tau) = 1.03e^{-45.7\tau}$. It is shown, slightly shifted for clarity, as the linear curve in the inset.

well estimated. This test establishes the performance of the AML algorithm and validates the velocity measurement presented above.

As a first validation of the entire particle-tracking technique as a Lagrangian measurement in turbulence, we compute the autocorrelation coefficient of the velocity fluctuations (one component only of the particle velocity is measured here)

$$\rho_v^L(\tau) = \frac{\langle v_x(t)v_x(t+\tau) \rangle_t}{v_{\text{rms}}^2}. \quad (34)$$

As shown in Fig. 11, the decrease of the velocity correlation is remarkably well fitted by an exponential form. We obtain $\rho_v^L(\tau) = 1.03e^{-\tau/T_L}$ with $T_L = 17$ ms. This behavior is in agreement with previous observations in direct numerical simulations of homogeneous isotropic turbulence [POPE]; the integral time T_L is characteristic of the flow forcing (energy injection).

V. CONCLUDING REMARKS

As can be seen in the previous section, both methods, time-frequency analysis and parametric spectral analysis, are suited for extracting the time-varying frequency modulation due to a Doppler effect. The domain of application of each method depends on the degree of nonstationarity and on the SNR.

For high SNR and weakly nonstationary signals, the time-frequency approach yields very good results. One drawback is the need of a second processing stage to extract the trajectory from the time-frequency picture. This stage may become increasingly difficult if there is more than one spectral component or if the SNR degrades. In both cases the quadratic nature of the algorithm produces interference patterns in the image: spurious clusters and a lacunar trajectory result. Another, more fundamental, limitation is that the length of the time window must be long enough to preserve an acceptable frequency resolution, even with the reassigned spectrogram. This limits the methods to weakly nonstationary signals.

For signals with a rapid frequency modulation, the AML spectral estimation is well suited, as long as the noise is near iid. The size of the time window can be decreased because of the parametric nature of the method, since *a priori* knowledge has been taken into account. The performance is further increased by the use of a Kalman-type filter. The drawback is the necessity to find a good dynamical model for the evolution of the spectral components. We have chosen here the simplest model which works well for our experiments, but the approach can be refined by increasing the number of parameters in order to consider more precisely the variation of the frequency. The AML algorithm also provides a quantitative estimation of the quality of the demodulation and the instantaneous power of the spectral component. It has the advantage to provide directly the frequency modulation as a function of time, in one stage.

The association of a Doppler acoustic technique with time-frequency or high-resolution parametric signal-processing algorithms yields a resolved measurement of single-particle velocities. We have validated this approach in two extreme cases; one example where an object moves in a quiet fluid and one example where the object is set into motion by turbulence. In both cases, the motion of the particle is successfully tracked. This new technique has potential applications in the tracking of solid bodies entrained (or propelled) in complex flows at low or high Reynolds numbers.

ACKNOWLEDGMENTS

We are indebted to Pascal Metz for the development of the signal conditioning electronics. We thank Marc Moulin for his help in the design of the von Kármán setup, VERMON for continuous assistance in the development of the transducer array. This work is partially supported by ACI Grant No. 2226.

APPENDIX: AML ALGORITHM

- (1) First step: calculate $\hat{\mathbf{R}}_x$ using the following expression:¹⁹

$$\hat{\mathbf{R}}_x = \frac{1}{2Q} \sum_{i=t+1}^{t+Q} (\mathbf{X}(i)\mathbf{X}(i)^T + \tilde{\mathbf{X}}(i)\tilde{\mathbf{X}}(i)^T), \quad (\text{A1})$$

with

$$\tilde{\mathbf{X}}(i) = [x(i+K-1), x(i+K-2), \dots, x(i)]^*T, \quad (\text{A2})$$

where * stands for complex conjugate. $\tilde{\mathbf{X}}\mathbf{X}$.

- (2) Second step: diagonalize $\hat{\mathbf{R}}_x$; one obtains the eigenvectors $(\mathbf{V}_i)_{i=1,\dots,K}$ and eigenvalues $(\lambda_i)_{i=1,\dots,K}$ sorted in decreasing order.
- (3) Third step: Compute $\hat{\Pi}_n$ and $\hat{\sigma}^2$, using the set of equations

$$\hat{\Pi}_n = \sum_{i=M+1}^K \mathbf{V}_i \mathbf{V}_i^T, \quad (\text{A3})$$

$$\hat{\sigma}^2 = \frac{1}{K-M} \text{Tr}(\hat{\Pi}_n \hat{\mathbf{R}}_x) = \frac{1}{K-M} \sum_{i=M+1}^K \lambda_i. \quad (\text{A4})$$

- (4) Fourth step: choose $\mathbf{F} = \hat{\mathbf{F}}(t)$ as a candidate value. Compute \mathbf{grad} and \mathbf{H} using¹⁸

$$\mathbf{grad} = \frac{2Q}{\sigma^2} \text{Re}\{\text{Diag}(\mathbf{S}'^+(\mathbf{F}) \cdot \Pi_n(\mathbf{F}) \cdot \hat{\Pi}_n \cdot \mathbf{S}(\mathbf{F}) \cdot \hat{\mathbf{P}})\}, \quad (\text{A5})$$

$$\mathbf{H} = \frac{2Q}{\sigma^2} \text{Re}\{\text{Diag}((\mathbf{S}'^+(\mathbf{F}) \cdot \Pi_n(\mathbf{F}) \cdot \hat{\Pi}_n \cdot \Pi_n(\mathbf{F}) \cdot \mathbf{S}') \star \hat{\mathbf{P}}^*)\}, \quad (\text{A6})$$

where the operator \star stands for the term to term matrix multiplication, and \mathbf{P}^* is the conjugate of \mathbf{P} , and

$$\mathbf{S}' = \left[\frac{d\mathbf{S}_1}{df_1}, \dots, \frac{d\mathbf{S}_M}{df_M} \right]^T. \quad (\text{A7})$$

- (5) Fifth step: using Eqs. (27)–(30), compute $\hat{\mathbf{F}}(t+1)$ and $\Gamma(t+1)$.

The initialization of the algorithm is done by either (i) setting an initial value of $\mathbf{F}(1)$ or (ii) estimating this value using the maxima of the amplitude of the FFT of a small window of signal (of length 64 or 128 samples) and using the iterative algorithm described in Sec. III B 3 to converge towards $\mathbf{F}(1)$.

For example, the extracted velocity of Fig. 9 is obtained by starting at the maximum energy of the signal and applying the algorithm forward and backward in time. The algorithm is stopped, as the mean of the inverse square root of the Hessian over a window of size 400 samples exceeds 0.5 for more than 400 samples.

¹G. O. Fountain, D. V. Khakhar, I. Mezic, and J. M. Ottino, *J. Fluid Mech.* **417**, 265–301 (2000).

²P. K. Yeung and S. B. Pope, *J. Fluid Mech.* **207**, 531–586 (1989).

³K. D. Squires and J. K. Eaton, *Phys. Fluids A* **3**, 130–143 (1991).

⁴P. K. Yeung, *Phys. Fluids* **6**, 3416–3428 (1994).

⁵P. K. Yeung, *Phys. Fluids* **9**, 2981–2990 (1997).

⁶M. Virant and T. Dracos, *Meas. Sci. Technol.* **8**, 1539–1552 (1997).

⁷G. A. Voth, K. Satyanarayan, and E. Bodenschatz, *Phys. Fluids* **10**, 2268–2279 (1998).

⁸O. F. Bay and I. Güler, *J. Med. Syst.* **23**, 77–84 (1999).

⁹P. Flandrin, *Time-Frequency/Time Scale Analysis*, Wavelet Analysis and its Application, Vol. 10 (Academic, New York, 1998).

¹⁰L. Cohen, *Time-Frequency Analysis*, edited by A. V. Oppenheim (Prentice-Hall, Englewood Cliffs, NJ, 1995).

¹¹G. Gaunard and H. Uberall, *J. Acoust. Soc. Am.* **73**, 1–12 (1983).

¹²P. D. Thorne, T. J. Brudner, and K. R. Waters, *J. Acoust. Soc. Am.* **95**, 2478–2487 (1994).

¹³B. T. Hefner and P. L. Marston, *J. Acoust. Soc. Am.* **107**, 1930–1936 (2000).

¹⁴R. Gendrin and C. de Villedary, *Ann. Telecommun.* **35**, 122–130 (1979).

¹⁵F. Auger and P. Flandrin, *IEEE Trans. Signal Process.* **43**, 1068–1089 (1995).

¹⁶S. Kay, *Modern Spectral Estimation, Theory and Application*, Prentice-Hall Signal Processing Series, edited by A. V. Oppenheim (Prentice-Hall, Englewood Cliffs, NJ, 1988).

¹⁷H. Clergeot and S. Tressens, in ICASSP'90, Albuquerque, NM (1990).

¹⁸O. Michel and H. Clergeot, in ICASSP'91, Toronto, Canada (1991), pp. 1277–1280.

¹⁹O. Michel, Ph.D. thesis, Université Paris XI, Orsay (1991).

²⁰A. Ouamri, Ph.D. thesis, Université Paris-Sud, Orsay (1986).

²¹It is straightforward to establish that $\Pi_s \mathbf{Y} = \mathbf{Y}$ for any vector \mathbf{Y} lying in the signal subspace. Here, “parametric projector” must be understood as the projector calculated for the vector of frequencies \mathbf{F} .

- ²²This is generally not the case, but this assumption remains valid as long as the log likelihood is well approximated by its second-order expansion around $\hat{\mathbf{F}}$.
- ²³M. R. Maxey and J. J. Riley, *Phys. Fluids* **26**, 883–889 (1983).
- ²⁴C. J. Lawrence and R. Mei, *J. Fluid Mech.* **283**, 307–327 (1995).
- ²⁵N. Mordant and J.-F. Pinton, *Eur. Phys. J. B* **18**, 343–352 (2000).
- ²⁶U. Frisch, *Turbulence, the Legacy of A. N. Kolmogorov* (Cambridge University Press, Cambridge, 1995).
- ²⁷A. L. Porta, G. A. Voth, A. M. Crawford, J. Alexander, and E. Bodenschatz, *Nature (London)* **409**, 1017–1019 (2001).
- ²⁸J.-F. Pinton and R. Labb, *J. Phys. II* **4**, 1461–1468 (1994).
- ²⁹J. Maurer, P. Tabeling, and G. Zocchi, *Europhys. Lett.* **26**, 31–36 (1994).
- ³⁰A. Arneodo, C. Baudet, F. Belin, R. Benzi, B. Castaing, B. Chabaud, R. Chavarria, S. Ciliberto, R. Camussi, F. Chill *et al.*, *Europhys. Lett.* **34**, 411–416 (1996).
- ³¹L. Scharf, *Statistical Signal Processing; Detection, Estimation and Time Series Analysis* (Addison-Wesley, Reading, MA, 1991).
- ³²Trademark, The Mathworks Company. The time-frequency toolbox can be downloaded at <http://crttsn.univ-nantes.fr/~auger/tftbftp.html>
- ³³L. Marié, J. Burguete, A. Chiffaudel, F. Daviaud, D. Eriher, C. Gasquet, F. Petielis, S. Fauve, M. Bourgoïn, M. Moulin, P. Odier, J.-F. Pinton, A. Guigon, JB Luciani, F. Namer, J. Léorat, in “Dynamo and dynamics”, Proceedings of the NATO Advanced Research Workshop, Cargèse (France), August 2000, NATO Science Series II Vol. 26; P. Chossat, D. Armbruster and I. Opera Eds. Kluwer Acad. Pub., Dordrech, The Netherlands (2001).